Research Square

Preprints are preliminary reports that have not undergone peer review.
They should not be considered conclusive, used to inform clinical practice,
or referenced by the media as validated information.

Spectral Recovery of Counterrotating Stellar Discs in TNG50

V.~S. Goradzhanov

vgoradzanov@gmail.com

Sternberg Astronomical Institute, Lomonosov Moscow State University

K.~O. Parfenov

P.~N.~Lebedev Physical Institute of the Russian Academy of Sciences

Research Article

Keywords:

Posted Date: November 26th, 2026

DOI: https://doi.org/10.21203/rs.3.rs-11732671/v1

License: This work is licensed under a Creative Commons Attribution 4.0 International License.
Read Full License

Additional Declarations: No competing interests reported.

Spectral Recovery of Counterrotating Stellar Discs in TNG50

V. S. Goradzhanov[1,2*] and K. O. Parfenov[3]

[1*]Sternberg Astronomical Institute, Lomonosov Moscow State University, Moscow, 119234, Russia.
[2]Faculty of Physics, Lomonosov Moscow State University, Moscow, 119991, Russia.
[3]Astro Space Center, P. N. Lebedev Physical Institute of the Russian Academy of Sciences, Moscow, Russia.

*Corresponding author(s). E-mail(s): vgoradzanov@gmail.com;

Abstract

We test the physical interpretation of spectral-model components using synthetic observations of six TNG50 galaxies with counterrotating stellar discs and four control galaxies. The spectra of two opposed apertures are fitted with the penalized pixel-fitting (pPXF) method using two or three Gaussian line-of-sight velocity distributions. We compare the recovered components with independently synthesized spectra of the retrograde families, their joint age–metallicity–velocity distributions, and their particle-based mean ages and masses. In fits to disc-system spectra without added noise, the relative error of the total spectrum is below 0.025%, whereas the spectral error of a component selected by velocity similarity ranges from 2 to 708%. A third profile improves joint-distribution recovery in 11 of 14 common apertures of five galaxies in this noiseless set. For the baseline spectra with added noise, it does not reduce the mean absolute age or mass error across galaxies. Mixtures of the original populations can reproduce some component spectra with substantially different retrograde flux fractions; the bounds depend on the source-family subdivision and spectral tolerance. Thus, an accurate total fit and agreement between the component masses from different models are insufficient to establish the component's physical identity.

Keywords: galaxies: kinematics and dynamics; galaxies: stellar content; methods: numerical; methods: statistical; cosmological simulations

1 Introduction

The ages and chemical compositions of counterrotating stellar discs are used to investigate galaxy assembly (Coccato et al. 2011; Johnston et al. 2013; Coccato et al. 2013, 2015). To measure these properties, multicomponent full-spectrum fitting represents the observed spectrum as stellar populations with separate line-of-sight velocity distributions (Cappellari 2017, 2023). The fitted template mixtures then provide an age and stellar mass for each component.

A single aperture can contain stars from several orbital families with overlapping velocities. The spectral model separates the combined spectrum into components whose ages and masses can differ from those of the dynamically defined stellar families. Interpreting a component as a counterrotating disc therefore requires a separate test. The detectability of counterrotation depends on the relative contributions, kinematics and observing conditions (Rubino et al. 2021). Photometric decomposition can supply additional information about the spatial contributions (Coccato et al. 2015; Tabor et al. 2019).

Synthetic observations of cosmological simulations allow inferred stellar populations to be compared with the properties of the original particles. The iMaNGA project analyses such TNG50 observations with pPXF for kinematics and FIREFLY for stellar populations (Nanni et al. 2022, 2023). Population estimates from pPXF have also been compared with TNG50 particles for total-galaxy and central spectra (Ikhsanova et al. 2025). General tools for synthetic integral-field spectroscopy are described, for example, by Bottrell and Hani (2022); Harborne et al. (2023).

Bugueño et al. (2026) studied counterrotating components and their origins in TNG50, selecting stars with circularity $\epsilon < -0.7$ within the main disc. Here the same circularity threshold is supplemented by requirements on resolution, structure and a distinct distribution peak to select systems for testing the spectral method.

We compare spectral-model components with the original retrograde families: their spectra, stellar age–metallicity–velocity distributions, mean ages and masses. We then determine which mixtures of physical populations are compatible with the fitted component spectra. This comparison tests the physical interpretation of the decomposition and assesses what changes from two velocity profiles to three. We also investigate sensitivity to observing conditions and population templates, the applicability of photometric constraints, and a mass-consistency check based on the spectral models alone.

2 Galaxies, synthetic observations and analysis

Two opposed apertures are selected from the synthetic images. Their spectra are fitted with a sum of stellar populations with different line-of-sight velocity distributions. The age and mass of the component selected by its similarity to the retrograde family are compared with particle-based reference values for the same aperture and spatial response.

2.1 Physical sample and reference populations

We use stellar particles from TNG50-1 at redshift zero, snapshot 99 (Pillepich et al. 2019; Nelson et al. 2019a,b). Their positions, velocities, ages, metallicities, initial masses and current masses retain their simulation values. Candidates come from the TNG50 supplementary stellar-circularity catalogue (Genel et al. 2015). Our particle census provides measurements of nonempty retrograde and prograde families for 7279 of its systems. The parent catalogue requires a stellar mass above $3.4 \times 10^8\ M_\odot$ within twice the stellar half-mass radius and at least 100 stars. Galaxies previously used to evaluate spectral or velocity-distribution procedures and their friends-of-friends groups are excluded. We include all six systems satisfying the disc criteria below, four control galaxies and two diagnostic systems. Selection uses physical properties and input availability before the new spectra are fitted. All 12 galaxies belong to distinct groups; Appendix A.1 gives the ranking rules.

The physical classification uses orbital circularity $\epsilon = J_z/J_{\rm circ}(E)$, with $E = \Phi + |\boldsymbol{v}|^2/2$. All bound stellar particles are sorted by E; $J_{\rm circ}$ is estimated by the largest J_z among the particle and its 50 neighbours on either side in this ordering, truncated at the ends. The z-axis of the galaxy coordinate system follows the current-mass-weighted stellar angular momentum within ten stellar half-mass radii. The optical radius $R_{\rm opt}$ is defined by the face-on, dust-free V-band surface brightness of 25 mag arcsec^{-2}. Classification uses a cylinder about the z-axis: $R \le R_{\rm opt}$, $|z| \le 5$ kpc. Here R is the distance from the z-axis and z is the height above the galaxy plane perpendicular to this axis. Within this cylinder, the retrograde family has $\epsilon < -0.7$ and the prograde family has $\epsilon > 0.7$. In six galaxies, the retrograde family meets our adopted criteria for a counterrotating disc: it contains enough particles, is spatially resolved, centred, flattened and rotationally coherent, and forms a distinct maximum in both the mass- and r-band-luminosity-weighted circularity distributions. Appendix A.1 gives the adopted criteria.

The primary quantities to recover are the retrograde family's current stellar mass and its arithmetic mean age weighted by r-band luminosity. For particle ages t_i and spatial weights a_i (Section 2.2), they are

$$M_{\rm CR,TNG} = \sum_{i \in \rm CR} a_i m_{i,\rm current}, \qquad t_{{\rm CR},r} = \frac{\sum_{i \in \rm CR} a_i L_{i,r}^{\rm BC03} t_i}{\sum_{i \in \rm CR} a_i L_{i,r}^{\rm BC03}}. \tag{1}$$

Here $L_{i,r}^{\rm BC03}$ is the luminosity assigned by the population-synthesis model of Bruzual and Charlot (2003), hereafter BC03. The current mass implied by BC03 is retained alongside the TNG particle mass to separate their mass normalizations.

Four control galaxies have a resolved prograde disc and lack both a qualifying retrograde peak and a resolved coherent retrograde family of the specified class. They can contain retrograde stars. Two diagnostic galaxies have resolved coherent retrograde families without a distinct peak and are evaluated separately from both classes. The six disc systems include four with a younger and two with an older retrograde family than the prograde family. These selection ages use intrinsic TNG r-band luminosities; the recovery targets in Eq. 1 use BC03 luminosities. The sample is designed to test the method on these galaxy classes. Table 1 lists its intrinsic properties.

Table 1 Intrinsic properties of the twelve validation galaxies.

ID	Group	N_-	$N_{\mathrm{eff},r}$	$M_\star$ [$10^{10} M_\odot$]	R_{opt} [kpc]	$\langle t \rangle_{r,-}$ [Gyr]	$\langle t \rangle_{r,\mathrm{bg}}$ [Gyr]	$100 f_{r,-}$ [%]
184947	D	21 717	5 510	0.621	5.5	4.25	8.18	27.7
514829	D	152 262	25 582	6.226	20.0	0.83	6.47	51.7
534628	D	69 438	10 280	5.017	14.0	1.66	7.53	25.4
651064	D	9 413	2 091	0.546	7.5	0.75	5.12	37.7
671812	D	11 390	10 615	0.429	10.5	7.57	2.73	7.09
671904	D	8 521	7 486	0.210	8.0	5.26	1.96	11.4
657721	C	122	77	0.503	12.0	8.49	3.36	0.075
632310	C	242	76	1.005	10.5	7.12	2.83	0.0687
621167	C	336	304	1.372	11.0	10.38	5.87	0.0997
580035	C	619	563	2.863	18.0	11.46	3.23	0.0513
96769	A	17 378	16 251	3.917	6.0	8.24	8.11	2.52
686190	A	2 114	1 711	0.443	4.0	3.76	4.15	2.83

D: six galaxies with a resolved counterrotating disc; C: four controls without a resolved disc of this class; A: two diagnostic systems with a coherently rotating retrograde family but no distinct retrograde circularity peak. All quantities refer to the intrinsic selection cylinder $R \leq R_{\mathrm{opt}}$, $|z| \leq 5$ kpc. The minus sign denotes stars with circularity $\epsilon < -0.7$; the background comprises all remaining stars in that cylinder. N_- is the number of these retrograde particles, and $N_{\mathrm{eff},r} = (\sum L_r)^2 / \sum L_r^2$ is their effective number, rounded to the nearest integer. $M_\star$ is the current stellar mass of all stars in the cylinder. The ages are linear means weighted by the original TNG r-band luminosities, and $f_{r,-} = L_{r,-}/L_{r,\mathrm{all}}$ is the relative luminosity of the retrograde stars in this band. R_{opt} is the intrinsic classification radius; observed apertures are defined separately from the synthetic images.

2.2 Synthetic images, apertures and spectra

Each star particle is represented by an interpolated BC03 simple stellar population (SSP), with a Chabrier initial mass function and normalization by its initial mass. Each particle's spectrum is Doppler-shifted according to its line-of-sight velocity and multiplied by the spatial-response weight. All gravitationally bound stellar particles contribute, including stars outside the classification cylinder whose light enters an aperture through the point-spread function (PSF). Family labels enter only the construction of separate reference spectra and the evaluation of fitted components.

We place the galaxies at luminosity distance $D_L = 100$ Mpc and observe the rest-frame interval 4800–5380 Å. The Gaussian line-spread function (LSF) has full width at half maximum (FWHM) 4.2 Å and the circular Gaussian PSF has FWHM 2.1 arcsec (0.974 kpc). The spectral interval and resolution are based on SAURON (Bacon et al. 2001; Emsellem et al. 2004); the adopted response is an idealized stellar-continuum observation with dust attenuation and gas emission omitted. Spatial samples are 0.94 arcsec across and the logarithmic spectral sampling is 69.03 km s^{-1}. Inclinations of 60 and 80 degrees provide two views at the same azimuth.

A separate 1800-s image with 0.47-arcsec pixels in the same spectral window, with independent noise, is used for aperture selection and photometric decomposition. An initial single-Sérsic fit supplies the background estimate. After subtracting this background, image moments determine the centre and position angle. The observed half-light radius $R_{50,\mathrm{obs}}$ is measured from the curve of growth: the integrated flux within nested elliptical apertures as a function of their semimajor axis. It is the semimajor axis enclosing half the total counts within the smallest of these ellipses that

encloses the detected region. Negative background-subtracted counts are retained in the sum. If the Sérsic fit does not converge, the aperture geometry is not determined. Two opposed rectangular apertures follow the observed major axis from $1.0R_{50,\mathrm{obs}}$ to $1.5R_{50,\mathrm{obs}}$, with transverse half-width $0.25R_{50,\mathrm{obs}}$. Geometry is measured at a segmentation threshold of three times the median pixel uncertainty. Across thresholds of two, three and five times this uncertainty, the radius range divided by its median must not exceed 0.20, the position-angle spread 10°, and the centroid spread 0.1 times the median radius. The detected region and apertures must lie inside the image, and each aperture must contain at least four fitting-pixel centres. Otherwise, spectra from that view are unavailable.

The exposure settings are 4×1800 and 16×1800 s. At each setting, we fit the expected spectrum without added noise and three independent noisy realizations. These realizations illustrate variability but are insufficient to calibrate failure probabilities or error distributions. Photon noise from the object and sky, detector read noise and the finite sky measurement determine the spectral uncertainties; both apertures share the measured sky. The spectra without added noise retain the same mean signal at the two exposures and have different uncertainty weights. The count model and observing parameters are given in Appendix A.2.

Separate resolution comparisons change the PSF FWHM to 1.5 arcsec or the spectral FWHM to 6.0 Å, one at a time, for spectra without added noise at 60 degrees and 4×1800 s. They retain the baseline observed aperture geometry. The 6.0 Å setting is based on the resolution of CALIFA V500 (Sánchez et al. 2016); other CALIFA observing parameters are not reproduced here. The particle-based target is recalculated for each spatial response, separating a change in the sampled population from a change in its recovery.

2.3 Spectral decomposition

We fit the spectrum of each aperture with the penalized pixel-fitting (pPXF) package, version 9.5.0 (Cappellari 2017, 2023), using one, two or three Gaussian line-of-sight velocity distributions, denoted 1G, 2G and 3G. The main comparison treats 2G and 3G as prespecified models; a criterion for selecting the number of components from the spectrum is not calibrated here. The single-component model is also used for isolated spectra of the retrograde family. Each component has its own nonnegative mixture of 90 BC03 SSP templates, velocity and dispersion. The templates span 15 ages from 0 to 13.8 Gyr and six metallicities from $Z = 0.0001$ to 0.05. The model is

$$S_{\mathrm{mod}}(\lambda) = P(\lambda) \sum_{k=1}^{K} \left[\sum_{j} w_{kj} T_j(\lambda) \right] \otimes G(v_k, \sigma_k), \qquad w_{kj} \geq 0. \tag{2}$$

Here T_j is an SSP spectrum normalized to unit mean luminosity density in the fitted window, w_{kj} is its absolute optical amplitude in component k, and $G(v_k, \sigma_k)$ is the component's Gaussian velocity distribution. A common degree-two multiplicative Legendre polynomial P, with its constant coefficient fixed to unity, describes smooth continuum differences. No additive polynomial or population regularization

is used. The templates include instrumental broadening. Velocities are bounded by ± 1000 km s^{-1} and intrinsic dispersions by 1–500 km s^{-1}. After fitting, we identify which model component corresponds to the retrograde family in velocity distribution.

The fitted SSP weights give current stellar masses and arithmetic mean ages weighted by r-band luminosity before the continuum polynomial is applied; Appendix A.3 specifies the conversion. We use multiple initial velocities and dispersions. Among all trial solutions with a finite full χ^2, we select the one with the lowest χ^2; the 3G search also includes the nested 2G candidate. If the search that produced the selected minimum did not converge, the result is rejected even when another trial converged. At least one converged trial with the requested number of components is also required, together with finite nonnegative weights. Numerical failures are counted separately from failures to match a component uniquely to the retrograde family.

2.4 Photometric information

We test whether image decomposition provides usable constraints on component contributions within the spectral apertures, following the principle of Coccato et al. (2015). We model the image as the sum of a Sérsic profile and one or two exponential profiles. A single Sérsic model provides the comparison for deciding whether a more detailed decomposition is supported. The profiles share a centre but have separate scales, flattenings and position angles. Each model is convolved with the PSF and fitted with a constant sky level.

The second exponential is retained only if it improves the Bayesian information criterion (BIC) by at least 10. The selected model must improve the single-Sérsic BIC by at least 10 and have reduced $\chi^2 \leq 1.5$. We also require $Q_{\rm loc} \leq 2$, where $Q_{\rm loc}$ is the mean squared standardized residual in pixels whose modelled source signal exceeds three times their uncertainty. Each profile must supply at least 5% of the modelled source counts, and nonlinear parameters must avoid their bounds.

2.5 Linking fitted components to the original stars

First, we select the model component to compare with the retrograde family. Its original velocity distribution is compared with the fitted Gaussians jointly in both apertures. Each aperture must have a uniquely closest profile with the same mean-velocity sign as the retrograde family; the joint selection must also be unambiguous and reproduce the reversal of mean line-of-sight velocity between apertures. The sum of the remaining profiles is compared with the velocity distribution of all stars outside the retrograde family. Appendix A.4 gives the full conditions. A comparison requires this match, an accepted numerical fit and finite age and mass estimates; it imposes no threshold on their errors.

We test the physical content of the fitted component in three ways. First, its spectrum $C_k(\lambda)$ is compared directly with the independently synthesized spectrum of the retrograde family, $S_{\rm CR}(\lambda)$, for the same aperture and PSF. The sum of the remaining components is compared with the spectrum of all other stars. We measure integrated flux, the relative residual norm $\|(C_k - S_{\rm CR})/s\|_2 / \|S_{\rm CR}/s\|_2$, and the shape difference after a single scalar normalization; $s(\lambda)$ is the assigned uncertainty of the

total spectrum. The model spectra include the common multiplicative polynomial. We also test sums of two 3G profiles. Selecting the best sum against the known true spectrum diagnoses what the saved solution can represent.

We then compare the joint distributions of age, metallicity and line-of-sight velocity. The original particles retain their physical properties and spatial weights. Each model component is represented by its SSP weights and Gaussian velocity distribution. The distributions are mapped to a common grid and normalized to unity. Their difference is measured by the total variation distance

$$D_{\mathrm{TV}} = \frac{1}{2} \sum_{b} |p_b - \widehat{p}_b|, \tag{3}$$

where p_b and $\widehat{p}_b$ are the normalized weights of the original family and the model component in the common bin b. This distance is zero for identical distributions and unity for disjoint distributions. The primary comparison uses r-band luminosity weights; the error in the overall normalization is assessed separately. Appendix A.5 describes the grid and the test with coarser bins.

Finally, we determine which mixtures of the original physical populations are simultaneously compatible with all fitted component spectra. The original stars are divided into four families: retrograde, prograde, the remaining stars inside the classification cylinder, and stars outside it. In the refined version, each family is further divided by age, metallicity and velocity. The spectrum of each part is synthesized from the original particles. Its flux can be allocated among components, but the total contribution of that part must be conserved. For a specified maximum residual in every spectral pixel, we find the smallest and largest retrograde flux fractions in the selected component. We use tolerances of $0.01s$, $0.1s$ and s, fixed before the calculation. The absence of an admissible mixture is retained as a separate outcome.

The three tests use spectra without added noise at both inclinations, with the baseline PSF and LSF and an exposure of 4×1800 s. They cover 48 solutions for the six disc systems and 28 for the controls. A further 20 planned solutions are unavailable because of aperture selection. For mass, we also use an identity separating the flux ratio, the mass-to-flux ratio and the BC03-to-TNG mass normalization (Appendix A.6).

Two diagnostics use the spectral fits alone. The first is the presence of opposite-sign velocity profiles in each aperture. The second checks mass consistency between 2G and 3G: their components are matched by the fitted velocity profiles, without information about the original particles. If $|\log_{10}(M_{2G}/M_{3G})| > 0.3$ dex, the difference triggers a warning and the 2G mass estimate is rejected; otherwise it is retained. Appendix A.7 defines both diagnostics.

Error changes between models use only observations with a matched component in both. Counts distinguish these common cases from estimates available in only one model, numerical failures and unavailable apertures. Appendix B.1 examines the sensitivity of the selected solutions to the uncertainty scale, initial guesses and matching tolerance. Summaries are first made by galaxy: views, apertures and noise realizations are repeated observations of the same physical object.

3 Recovering the retrograde population

3.1 Populations sampled by the observations

Apertures satisfying the adopted geometry criteria can be defined for 19 of the 24 projected images, providing 38 of the 48 planned apertures. These include both views of all six counterrotating-disc systems and seven views of the four control galaxies. Both diagnostic galaxies have apertures that are too small under the adopted sampling criterion; the single-Sérsic fit does not converge for control galaxy 621167 at 80°. These cases remain unavailable in the spectral comparisons.

The physical populations contribute very differently to the observed spectra (Fig. 1). The retrograde family supplies 34–86% of the optical flux in the four systems with a younger retrograde population, but only 0.36–6.5% in the two with an older one. Its fraction is below 0.06% in the four control galaxies. Thus the age categories also differ in spectral contrast. Their recovery errors cannot isolate an effect of age from that of population mixing and the other differences between galaxies. At 4×1800 s, the expected signal-to-noise ratios in the apertures of the six disc systems range from 12 to 136 per spectral sample, expressed as the median over wavelength. Increasing the exposure to 16×1800 s doubles this expected ratio under the adopted noise model.

3.2 Component spectra and stellar distributions

Of the 48 disc-system solutions without added noise at the two inclinations, 47 pass the numerical checks. Both synthesis and fitting of these spectra use the BC03 library. In all these solutions, the relative total-spectrum residual norm is below 0.025%. For the 38 components matched to the retrograde family, however, the relative spectral error ranges from 2.0 to 708%. Excess or missing flux in the selected component is almost entirely cancelled by the opposite error in the remaining components: the total residual norm is 0.012–0.595% of the sum of the norms of these two errors. The accuracy of the total spectrum therefore provides only a weak constraint on its separation into physical populations.

In five of the 23 numerically admissible 3G solutions, the retrograde family's spectrum is better reproduced by the sum of two profiles than by any single profile. Four cases belong to 514829: the relative error falls from 13.8–32.0% for the best single profile to 1.7–2.4% for the pair. The fifth case is one aperture of 651064. This selection uses the known true spectrum and shows the limitation of representing the family by one component in that solution.

Figure 2 shows flux recovery and a paired comparison of joint age–metallicity–velocity distribution errors in 2G and 3G. The kinematic matching conditions are met by 20 of the 24 2G solutions and 18 of the 24 3G solutions. Among the 14 common apertures of five galaxies, the total variation distance D_{TV} (Eq. 3) decreases in 11 cases. The mean of the within-galaxy medians of $D_{\mathrm{TV},3G} - D_{\mathrm{TV},2G}$ is -0.084; with coarser bins, it is -0.083. For this paired set, the third profile improves the description of the population distribution. After summing over velocity bins, the joint age–metallicity distribution also improves in 11 of the 14 apertures. The separate age

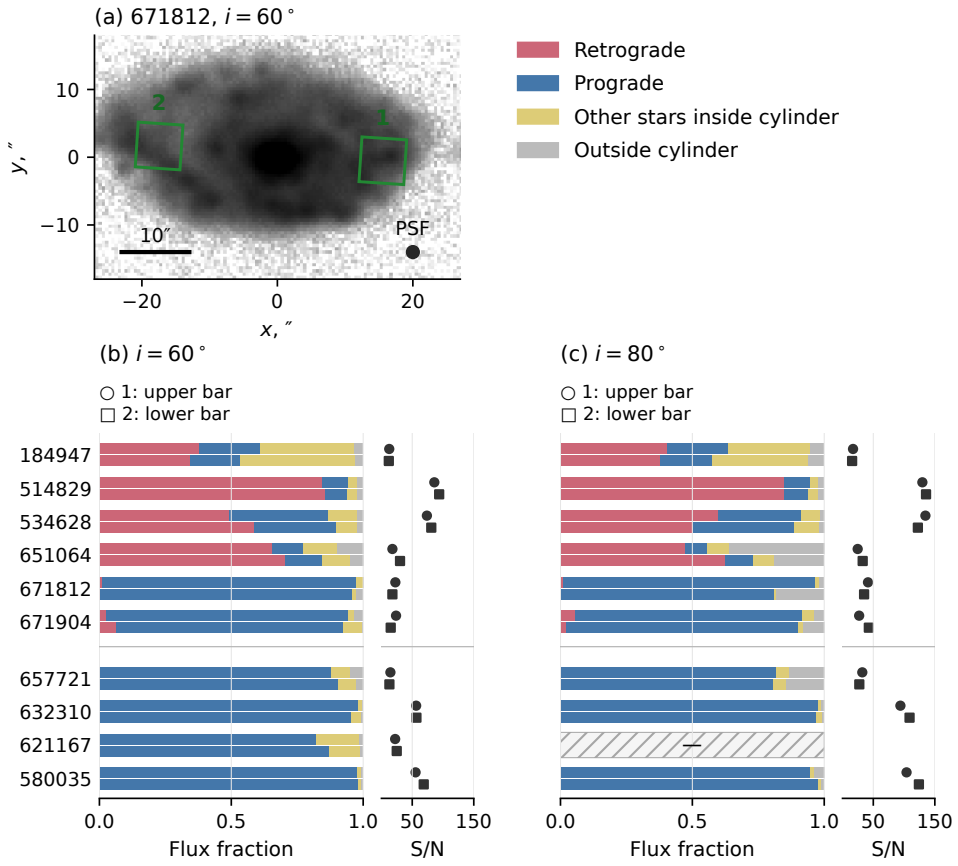


Fig. 1 Apertures and contributions of stellar families to the observed flux. (a) Synthetic image of galaxy 671812 at $i = 60^\circ$ over the adopted spectral window: green outlines mark apertures 1 and 2, and the circle marks the 2.1″ PSF FWHM. The image has 0.47″ pixels and is shown after subtraction of the prescribed sky with a nonlinear stretch. Coordinates are measured from the original image centre. Apertures 1 and 2 lie on the negative and positive sides of the photometric major axis, whose positive direction points left here. (b, c) Flux fractions of four disjoint stellar families over 4800–5380 Å for the ten galaxies with available spectra. Upper bars and circles correspond to aperture 1, lower bars and squares to aperture 2. Points on the right give the median S/N per spectral sample for 4×1800 s. The horizontal line separates six counterrotating discs from four controls. Hatching marks the unavailable projection of 621167. Both projections of the two diagnostic systems are unavailable; 38 of 48 planned apertures are available in total.

and metallicity distributions improve in 10 and 13 apertures, respectively; all these comparisons use r-band luminosity weights.

A smaller flux error does not ensure equally accurate population recovery. In the first aperture of 184947 at $i = 60°$, moving from 2G to 3G changes the component-to-true optical flux ratio from 1.210 to 1.030 and the r-band luminosity ratio from 1.204 to 1.027. Yet D_{TV} changes little: 0.255 and 0.257. In both models, the recovered stellar distribution remains appreciably different from the original one.

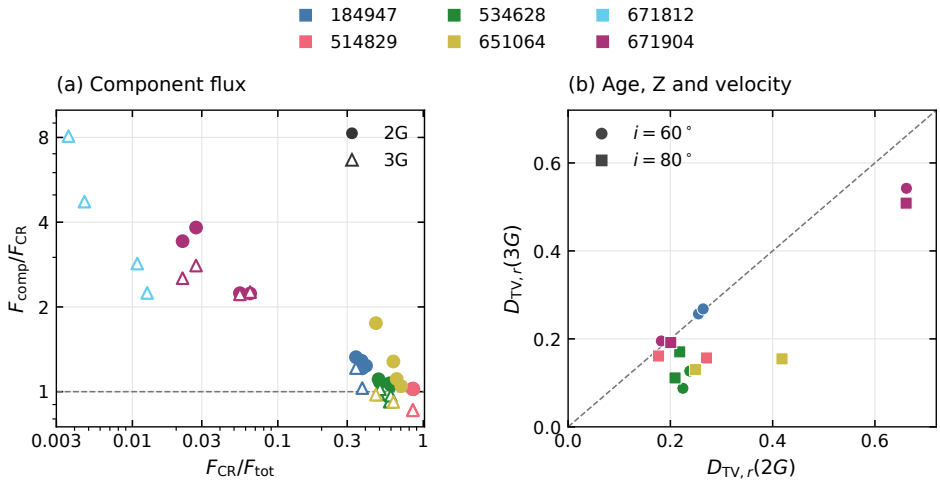


Fig. 2 Recovery of the selected component in spectra without added noise at 4×1800 s and inclinations of 60° and 80°. (a) Fitted component flux relative to the true retrograde-family flux versus the family's fraction of the total aperture flux; the horizontal line marks exact flux recovery. Shown are 20 of the 24 planned 2G components and 18 of the 24 planned 3G components that pass kinematic matching. (b) Comparison of the total-variation distances $D_{\mathrm{TV,r}}$ between the normalized joint age–metallicity–velocity distributions of the fitted component and the retrograde family, weighted by r-band luminosity. Each point represents one of 14 common apertures in five galaxies; points below the diagonal favour 3G. Colours identify galaxies; symbol shapes are defined separately in each panel.

In the second aperture of 671904 at 80°, the 2G model reproduces the total spectrum with a relative error of 0.0125%, while the selected component has 3.42 times the retrograde family's flux (Fig. 3).

3.3 Physical mixtures compatible with the components

We compared two representations of the source stellar families: one summed spectrum per family and a set of subgroup spectra separated by age, metallicity and velocity. In the first case, redistributing flux among components preserves the internal proportions of each family; in the second, the subgroups can be redistributed independently. A tolerance of $0.1s$ limits the difference between a model component and its mixture in every spectral pixel to one tenth of the assigned uncertainty $s(\lambda)$ of the full input spectrum.

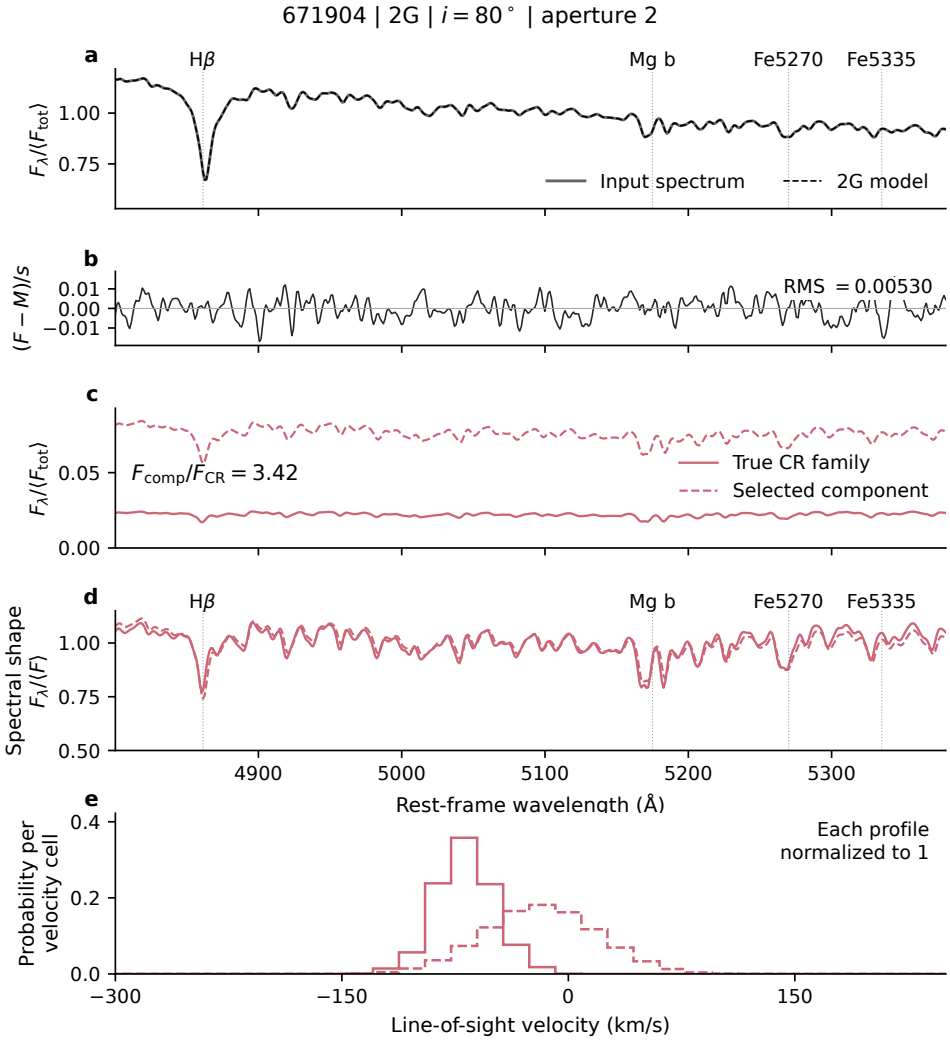


Fig. 3 Spectral decomposition of galaxy 671904, aperture 2, $i = 80°$, with the 2G model. No noise was added to the spectrum; both synthesis and fitting use BC03 templates. (a) Input spectrum and full model, indistinguishable at this scale. (b) Their difference divided by the prescribed total-spectrum error s; RMS$[(F - M)/s] = 0.00530$. (c) The retrograde-family spectrum (solid) and the selected fitted component (dashed). Panels (a) and (c) are normalized by the mean flux of the full input spectrum; the component flux exceeds the true value by a factor of 3.42. (d) The same two spectra divided by their respective means. Labels mark stellar absorption features on the air-wavelength scale in the galaxy rest frame. (e) The true retrograde velocity distribution weighted by optical spectral luminosity and the selected Gaussian profile, each normalized to unity on the original velocity grid.

At this tolerance, replacing the four summed spectra with subgroup spectra increases the number of compatible solutions from 9 to 17 among the 38 kinematically matched components (Table 2). In 16 of these 17 cases, the upper bound on the retrograde flux fraction is below unity: describing the selected component requires contributions from other families as well.

For the first aperture of 184947 at 60°, the four summed spectra give a retrograde flux-fraction range of 0.824–0.825 in 2G. At the same tolerance of $0.1s$, subgroup spectra broaden it to 0.753–0.832. In 3G, no mixture of the four summed spectra meets this tolerance, whereas subgroup spectra give a range of 0.697–0.984. Allowing subgroup fluxes to be assigned independently among components thus changes the composition bounds substantially.

At a tolerance of s, the subgroup-spectrum ranges in the same example broaden to 0–0.966 for 2G and 0–1 for 3G. For three of the 18 selected 3G components, the admissible flux can vanish and the retrograde flux fraction is undefined. At the strictest tolerance, $0.01s$, no admissible mixture exists for any of the 75 numerically admissible disc and control solutions.

Table 2 Physical-mixture test: component counts in each category among the 20 matched 2G components and 18 matched 3G components. "Range found" means that an admissible mixture exists and the bounds on the retrograde flux fraction are defined. "Zero flux" means that the component flux can vanish, leaving the fraction undefined. "No mixture" means that no mixture of the source spectra meets the tolerance. All components of each model are described simultaneously, preserving the total contribution of every source spectrum.

Source spectra	Model	Tolerance	Number of components		
			Range found	Zero flux	No mixture
4 families	2G	$0.1s$	6	0	14
	3G	$0.1s$	3	0	15
Up to 48 subgroups	2G	$0.1s$	10	0	10
	3G	$0.1s$	7	0	11
4 families	2G	s	20	0	0
	3G	s	13	3	2
Up to 48 subgroups	2G	s	20	0	0
	3G	s	14	3	1

3.4 Age and mass errors

In this and the following comparisons, the primary regime is $i = 60°$ and an exposure of 4×1800 s; other conditions are stated explicitly. We first take the median error over the included apertures and realizations of each galaxy, then average these medians with equal galaxy weights. Changes in absolute error are summarized in the same way, pairing the same aperture and realization between the two models.

Table 3 gives the errors for each of the six galaxies relative to the retrograde family's r-band-luminosity-weighted age and current TNG mass in the same aperture. The four younger retrograde discs have 2G mass errors of +0.06–+0.12 dex. Recovery is poorer for the older discs: the median mass error is +0.31 dex for 671904, while no component can be selected for 671812.

Table 3 Baseline age and mass errors without added noise, at $i = 60°$ and an exposure of 4×1800 s. Each row gives the median signed error over N of the galaxy's two apertures with an accepted component match. The age error δt_r is the recovered minus true r-band-luminosity-weighted age; the mass error is $\delta \log M_* = \log_{10}(M_{\rm fit}/M_{\rm TNG})$ for current stellar mass. A dash denotes unavailable matching.

		2G			3G	
ID	$N/2$	δt_r (Gyr)	$\delta \log M_*$ (dex)	$N/2$	δt_r (Gyr)	$\delta \log M_*$ (dex)
184947	2/2	+0.74	+0.07	2/2	+0.26	+0.01
514829	2/2	+0.29	+0.06	0/2	—	—
534628	2/2	+0.62	+0.12	2/2	−0.18	−0.14
651064	2/2	+0.24	+0.07	0/2	—	—
671812	0/2	—	—	2/2	−0.57	+0.55
671904	2/2	−0.74	+0.31	2/2	−0.52	+0.26

The third profile allows a component to be matched to the family in 671812, but its median mass error reaches +0.55 dex. Matching is instead lost for 514829 and 651064: the component selected jointly across the two apertures is not closest to the retrograde distribution in at least one of them. Across the six common apertures of three galaxies, adding a profile reduces the absolute age error by an average of 0.38 Gyr and the absolute mass error by 0.018 dex. The improvement on the common set thus accompanies a change in which galaxies allow the selected component's properties to be evaluated.

With added noise, fewer estimates meet the comparison conditions, and they represent a different set of galaxies (Table 6). In the primary regime, 2G provides 14 such estimates from 36 noisy aperture spectra, and 3G provides 12. All belong to 514829, 534628 and 651064. For neither older retrograde family can the age and mass of a matched component be compared with the original population in any baseline noisy observation. In the 12 cases with estimates from both primary 2G–3G models, the mean change in absolute age error over the three galaxies is +0.084 Gyr and the mass change is +0.035 dex; two further estimates are available only with two profiles. Thus adding a profile does not reduce errors on average across galaxies in these noisy spectra.

The mass-error decomposition in Eq. 9 shows the role of flux. In the two apertures of 671812, the 3G mass errors are +0.36 and +0.73 dex. The model-to-retrograde-family flux-ratio term is +0.46 and +0.91 dex, respectively. Differences in mass-to-flux ratios and in the BC03 and TNG mass normalizations partly offset this excess.

All 12 isolated-family BC03 spectra in the primary regime yield numerically admissible age and mass estimates. Their true velocity distributions are approximated by a single Gaussian in the fits. Their maximum absolute errors are 0.562 Gyr and 0.067 dex. Thus a spectral population estimate can differ from the particle mean even without background contamination. The isolated spectra help interpret the mixture errors while the true family remains their physical reference.

3.5 Sensitivity to observing conditions and the model

Increasing exposure from 4 to 16 × 1800 s changes both the errors and the set of available estimates. On common noisy spectra at 60°, the absolute mass error, averaged over the two represented galaxies, decreases by 0.047 dex for 2G and increases by 0.014 dex for 3G. Age errors change little for 2G and increase for 3G. Both S/N and the noise realization change in this comparison; Table 6 gives the full counts of available estimates.

For spectra without added noise, longer exposure changes only the assigned uncertainties. Differences between results for the identical signal characterize the numerical search: in the most sensitive case, age shifts by 0.435 Gyr and mass by 0.048 dex (Appendix B.1). Changing the initial guesses for one disc and one control galaxy preserves their kinematic-matching outcomes.

Matched changes to the PSF or LSF have moderate effects on errors in common apertures, although some estimates become unavailable (Table 5). An incorrect LSF can have a larger effect: for an input FWHM of 4.2 Å and a model FWHM of 3.78 Å, the mean absolute 3G age error over four galaxies increases by 1.65 Gyr. In 671812 the age and mass errors reach −4.93 Gyr and +0.93 dex. The imposed 10% LSF offsets serve as a sensitivity test. A lower bound of 80 km s^{-1} on the third profile's dispersion preserves the total count (8/12), but replaces four apertures with others.

With E-MILES (Vazdekis et al. 2016), 4/12 apertures enter the comparison for 2G and 2/12 for 3G. For 3G, none coincides with the apertures available with BC03. All 12 isolated spectra yield estimates, but the two older families have age errors of +3.20 and +3.77 Gyr and mass errors near +0.27–+0.28 dex. This comparison changes the template spectra, the Chabrier initial mass function to a Salpeter initial mass function, and the minimum age to 0.0631 Gyr simultaneously. Using the optical weights defined in Appendix A.4, younger particles supply 10–41% of the retrograde contribution in three younger-disc systems and 17–31% of the prograde contribution in the two systems with older retrograde discs. The result therefore reflects the combined change in the population model.

3.6 Observable profiles and the mass-consistency check

Profiles with opposite signs of mean velocity appear in both apertures more often than a component can be matched to the retrograde family and its properties evaluated. In the primary regime without added noise the diagnostic is present in 5/6 disc systems for 2G and 6/6 for 3G, but in none of the four control galaxies. With noise it is present in 9/18 disc aperture pairs for 2G and 14/17 evaluable pairs out of 18 planned for 3G. In the control galaxies it appears in 5/12 noisy 3G pairs and in 0/12 for 2G. Thus,

in the tested noisy series, local signatures of opposite motion also occur in galaxies without a resolved counterrotating disc.

In two noisy 3G estimates for the control galaxy 632310, a component can be matched to its small retrograde family. The median age and mass errors are nevertheless −10.78 Gyr and +1.65 dex. Such a match alone therefore does not identify a resolved counterrotating disc.

The mass-consistency check can be applied to only some estimates (Fig. 4). For the six disc systems without added noise, baseline age and mass estimates are available in 10/12 apertures; masses can be compared between models in nine cases, of which seven pass the check. The only one of these nine estimates with a mass error above 0.3 dex also passes. For noisy spectra, the baseline estimates, evaluable checks and estimates passing the check number 14/36, 10/36 and 8/36, respectively. None of these eight has a mass error above 0.3 dex, but one has an age error above 1 Gyr. Another estimate with a large mass error cannot be checked in this way and is therefore absent from the set passing the check. These eight noisy estimates represent only two galaxies and do not determine the probability of missing a large error.

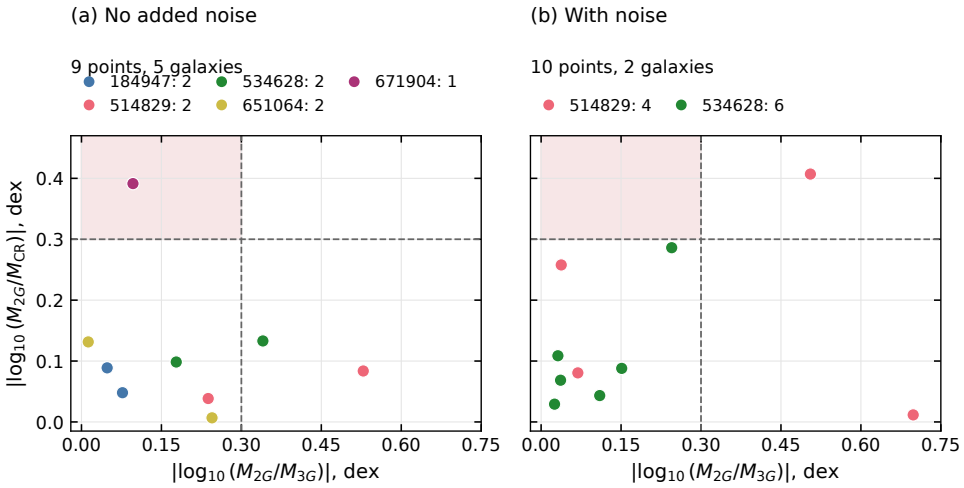


Fig. 4 Mass consistency between models versus the accuracy of the selected component mass at $i = 60°$ and 4×1800 s. The horizontal axis shows the mass difference between the 2G component and its kinematically matched 3G profile; the vertical axis shows the absolute 2G mass error relative to the true retrograde-family mass. Dashed lines mark the 0.3 dex thresholds. In the shaded region, agreement between models accompanies a large mass error. (a) Each point represents an aperture without added noise: 9 of 12 comparisons are evaluable, covering five galaxies. (b) Each point represents an aperture and a noise realization: 10 of 36 comparisons are evaluable, covering only two galaxies, 514829 (4 points) and 534628 (6 points). Colours identify galaxies; the legend numbers give the point counts.

3.7 Availability of photometric constraints

Photometric flux fractions could not be used to constrain the spectral models: none of the 24 images passed the quality criteria. The model comparison was completed for 23 views; the initial Sérsic model did not converge in the remaining view. In every completed comparison, adding exponential profiles improved BIC by at least 10, but the local residual exceeded $Q_{\rm loc} = 2$, including the four images with an acceptable global χ^2_ν. The local image structure remains insufficiently described, so the decomposition supplies no accepted photometric constraints for the spectral fits.

4 Discussion

4.1 Physical identification of spectral components

The direct comparisons reveal a substantial difference between reproducing the summed spectrum and recovering its physical populations. Opposing errors in the component spectra can nearly cancel in the sum. In the faint old disc 671812, the selected component receives excess flux and its mass is overestimated even without added noise. Differences in mass-to-flux ratios and mass normalizations partly offset the flux error, so a small mass error can also conceal an incorrect spectral contribution.

The joint age–metallicity–velocity distribution tests the recovered population beyond its mean age and total flux. Each fitted Gaussian shares one age–metallicity distribution across all velocities, whereas the original family can contain correlations between population and kinematics. The admissible-mixture calculation then asks which physical populations can supply the fitted component spectra while conserving the total flux of every source population. Together, these comparisons test the population interpretation of a component selected by velocity.

The composition bounds depend on the source spectra and the adopted spectral tolerance. Subdividing a family permits different contributions from its constituent populations and can widen the bounds. A broad range establishes ambiguity within the tested set; a narrow range requires checking its sensitivity to the source subdivision. In the selected galaxies, younger retrograde populations also have higher flux contrast than older ones, so this comparison cannot isolate the effect of age.

4.2 The effect of the number of components

A third Gaussian redistributes the spectrum among all components. In some noiseless solutions, the sum of two profiles reproduces the retrograde family's spectrum more accurately than any single profile. The third profile also improves the joint population distribution in most common apertures of the five galaxies entering that comparison.

Age and mass comparisons use observations in which both models allow a unique match to the retrograde family. On the common noiseless subset, the third profile reduces the absolute age error on average across galaxies; on the primary noisy subset, neither mean absolute age nor mass error improves. The third profile and its dispersion constraint also change which observations yield an estimate. Accuracy must therefore be assessed together with the fraction of available estimates. Distribution comparisons and composition bounds describe the selected spectral solutions; their stability

under renewed optimization remains unestablished given the numerical sensitivity to uncertainty rescaling (Appendix B.1).

The 2G and 3G mass estimates can agree with each other while both differ substantially from the true mass. The value of a mass-consistency check depends on the errors among retained estimates and their fraction among all planned observations. The absence of a comparable component in one model leaves the check unavailable.

4.3 Independent information and observing conditions

Spatial information can constrain component fluxes. Coccato et al. (2015) used a Sérsic bulge and two exponential discs for NGC 4191, while Tabor et al. (2019) matched bulge–disc photometric models to the spectroscopic PSF and spatial bins in MaNGA. Here, smooth image profiles fail the adopted quality criteria, mainly through local residuals. Images provide aperture geometry for most views but no accepted component flux constraints, so their effect on spectral recovery remains untested. Applying such constraints requires an adequate image model and a correspondence between its spatial components and the kinematic populations.

The exposure comparison combines a change in expected signal-to-noise ratio with independent noise draws and changes in which galaxies yield matched components. The direction of the error change depends on the model and estimated quantity. Spatial resolution also changes the stars contributing to an aperture, so its reference age and mass must use the same aperture and PSF. A mismatch in the assumed LSF can affect recovery more strongly than poorer spectral resolution with a correctly specified LSF. The ten per cent mismatch tested here illustrates this sensitivity; application to an instrument requires its measured LSF uncertainty.

Isolated-family spectra reveal population errors before mixing with other families, while retaining the original velocity distribution that the model approximates by a Gaussian. The E-MILES comparison changes the library, initial mass function and template age range together. Stars younger than its lower age limit contribute appreciably to several input populations. These differences already affect the isolated spectra; mixture fitting additionally requires allocating populations among velocity profiles.

4.4 Scope and relation to other methods

Synthetic-observation studies such as iMaNGA (Nanni et al. 2023) and the TNG50 mock WEAVE analysis of Ikhsanova et al. (2025) assess recovery of composite stellar populations. Our comparison with dynamically selected particle families extends the evaluation to the physical interpretation of individual spectral components. The contribution is the combined test of their spectra, population distributions and compatible physical mixtures, including components whose ages and masses cannot be evaluated under the adopted matching rule.

Zhu et al. (2020) already validated population–orbit superposition models against Auriga simulations, comparing recovered orbital and population distributions and the maps of individual orbital components with the original galaxies. Those models use spatially resolved kinematic and population maps. Applying the present component

tests to orbit-based models of TNG50 would require a separate analysis with those spatial constraints.

The conclusions concern a targeted sample and an idealized observation of stellar continuum. The two diagnostic systems have no usable apertures at the adopted distance and sampling. Controls demonstrate that local profiles with opposite velocity signs can occur without a coherent counterrotating disc. A selection procedure for a broader population would require more independent galaxies, wider spatial coverage and more noise realizations.

5 Conclusions

Synthetic observations with known particle populations make it possible to test what a spectral decomposition recovers. In the studied TNG50 galaxies, component errors can nearly cancel in a highly accurate total spectrum, and agreement between two- and three-profile mass estimates can retain a physically inaccurate result. A faint old disc has a mass overestimate reaching 0.7 dex.

Adding a third profile improves the joint population distribution in 11 of the 14 common apertures of five galaxies without added noise. It can also distribute the retrograde family's spectrum between two profiles and change whether a single corresponding component can be selected. In the primary noisy comparison, the mean absolute age and mass errors do not improve.

The allowed retrograde flux fraction depends on the subdivision of source populations and the spectral tolerance. Together with direct comparisons of component spectra and population distributions, these bounds identify improvements and remaining ambiguities in the decomposition. The recovery assessment includes errors in the matched components and cases where no component can be matched to the intended population.

Acknowledgements

We thank the IllustrisTNG collaboration for making the TNG50 simulation data publicly available.

We acknowledge the use of OpenAI Codex for assistance with developing and debugging the analysis code, designing validation checks, and drafting, translating and editing the manuscript. The authors take full responsibility for the scientific content and final manuscript.

A Criteria and physical evaluation

A.1 Physical-selection criteria

Control candidates are inspected in increasing retrograde current-mass fraction. Among those passing the control criteria, four are selected nearest the centres of the quartiles in current stellar mass within the classification cylinder. Diagnostic candidates satisfy the resolution, age-stability and structural requirements but lack a separate peak and have retrograde-minus-prograde mean-age differences between -1 and $+1$ Gyr. Their retrograde and intermediate-circularity ($|\epsilon| \leq 0.7$) relative r-band luminosities are converted to percentile ranks. We select the object nearest $(0.5, 0.5)$ and then the remaining object farthest from the first in this rank plane. Already selected groups are excluded.

Table 4 specifies the sampling, structure and circularity criteria used to select the physical families. The effective particle number is $N_{\mathrm{eff},r} = (\sum_i L_{i,r})^2 / \sum_i L_{i,r}^2$; $R_{50,r}$ encloses half the family's r-band luminosity. Structural measures use current-mass weights. The axis ratio c/a is the square root of the smallest-to-largest eigenvalue ratio of the centred position covariance. The azimuthal asymmetry is $m_1 = |\langle e^{\mathrm{i}\phi} \rangle|$ and angular-momentum coherence is $|\sum_i m_i \boldsymbol{j}_i| / \sum_i m_i |\boldsymbol{j}_i|$, where $\boldsymbol{j}_i$ is specific angular momentum. The velocity scale satisfies $\sigma^2_{\mathrm{global}} = [\mathrm{Var}(v_R) + \mathrm{Var}(v_\phi) + \mathrm{Var}(v_z)]/3$.

Table 4 Physical-selection criteria. Luminosity weights use intrinsic TNG r-band values. The younger and older categories correspond to retrograde-minus-prograde mean-age differences of at most -1 Gyr and at least $+1$ Gyr, respectively.

Criterion	Requirement or adopted value
Sampling and extent	At least 1000 particles, $N_{\mathrm{eff},r} \geq 1000$ and $R_{50,r} \geq 0.576$ kpc for each family; resolution and age category remain valid at retrograde cuts $-0.65, -0.70, -0.75$.
Disc structure	$c/a \leq 0.4$, centroid offset $\leq 0.1 R_{\mathrm{opt}}$, $m_1 \leq 0.2$, angular-momentum coherence ≥ 0.8, $\lvert\langle v_\phi \rangle\rvert / \sigma_{\mathrm{global}} \geq 2$ and retrograde–prograde angular-momentum angle $\geq 150^\circ$.
Circularity peak	Retrograde peak in both mass and r-band weightings: Gaussian smoothing width 0.10, peak at $\epsilon \leq -0.65$ and peak-to-valley ratio ≥ 1.5. Controls lack a peak at smoothing widths 0.05, 0.10 and 0.15 and lack a resolved stable coherent retrograde family.

A.2 Photon counts and spectral uncertainties

For an aperture covering $n = \Omega/(0.94\ \mathrm{arcsec})^2$ spatial samples, the expected variance in each spectral bin, in electron counts, is

$$\begin{aligned} V_\lambda &= S_\lambda + n(B_\lambda + R_\lambda^2) + \frac{n^2}{N_{\mathrm{sky}}}(B_\lambda + R_\lambda^2), \\ R_\lambda^2 &= \sigma_{\mathrm{read}}^2 n_{\mathrm{ext}} N_{\mathrm{exp}} \frac{\Delta\lambda_{\mathrm{obs}}}{\delta\lambda_{\mathrm{det}}}. \end{aligned} \tag{4}$$

Here S_λ is the expected object count, B_λ the sky count per spatial sample, and the final term accounts for estimating the common sky from $N_{\mathrm{sky}} = 146$ samples. We adopt collecting area 13.8544 m^2, throughput 0.20, read noise $\sigma_{\mathrm{read}} = 5$ electrons, $n_{\mathrm{ext}} = 5$ extraction pixels and detector sampling $\delta\lambda_{\mathrm{det}} = 1.1$ Å. The sky has constant f_ν and surface brightness 21.9 AB mag arcsec^{-2}. Object and sky counts follow $C_\lambda = A\eta t\, f_{\lambda,\mathrm{obs}} \Delta\lambda_{\mathrm{obs}} \lambda_{\mathrm{obs}}/(hc)$, with $t = N_{\mathrm{exp}}\, 1800$ s and $f_{\lambda,\mathrm{obs}} = L_{\lambda,\mathrm{rest}}/[4\pi D_L^2(1+z)]$ for the object. The observing redshift follows $D_L = 100$ Mpc in a flat cosmology with $H_0 = 67.74$ km s^{-1} Mpc^{-1} and $\Omega_m = 0.3089$.

Noisy spectra combine independent Poisson object-plus-sky and sky counts with Gaussian read noise. Their variance uses the measured object-plus-sky and total sky counts in place of their expectations. Both apertures share the same sky realization. The uncertainty $s(\lambda)$ is $\sqrt{V_\lambda}$ divided by the luminosity-to-count conversion; spectral samples are treated as independent.

A.3 SSP normalization and population estimates

Let ℓ_j be the mean instrumentally broadened luminosity density of SSP j per unit initial mass over the fitted pixels, μ_j its BC03 current mass per unit initial mass, and $l_{r,j}$ its r-band luminosity per unit initial mass. Templates are divided by ℓ_j. The input spectrum is divided by its mean a for fitting, and the returned pPXF coefficients u_{kj} are restored to absolute weights $w_{kj} = a u_{kj}$. Thus

$$M_k = \sum_j \frac{w_{kj}\mu_j}{\ell_j}, \qquad t_{k,r} = \frac{\sum_j w_{kj} l_{r,j} t_j/\ell_j}{\sum_j w_{kj} l_{r,j}/\ell_j}. \tag{5}$$

These estimates describe the population before multiplication by P. The component spectra and their integrated fluxes include P; its continuum correction is not interpreted as additional stellar mass.

A.4 Matching profiles to families

For evaluation, the complete particle population is partitioned into the retrograde family, the prograde family, the remaining stars inside the classification cylinder, and all stars outside it. The same spatial PSF–aperture response is applied to the particles of every group.

Matching to the original family uses optical weights: the mean rest-frame luminosity density in the spectral window before the velocity shifts. For normalized cell

probabilities p_b and g_b, we use the squared Hellinger distance $H^2 = 1 - \sum_b \sqrt{p_b g_b}$. We consider each possible choice of one Gaussian per aperture for the retrograde family. The chosen profile is compared with the original retrograde distribution, and the sum of the remaining profiles with the distribution of all other stars. The mean of these four distances, two per aperture, measures the difference for the joint choice. We first exclude choices in which either the selected component or the sum of the others fails to reverse its mean-velocity sign between apertures. Among the remaining choices, the distance must have a unique minimum. In each aperture, the chosen profile must also be closest to the retrograde distribution. In both comparisons, its advantage over the next-best choice must exceed the numerical tolerance of 10^{-6} in the corresponding distance measure. The chosen profile must have positive amplitude and the same mean-velocity sign as the family. Both aperture fits must pass the numerical checks. Gaussian tails outside the velocity grid are included in the comparison. The tolerance excludes nearly equal values but does not define statistical confidence or selection robustness.

A.5 Joint distribution and admissible composition

The ages and metallicities of particles and SSP templates are projected onto the same native BC03 grid using the log-age and log-metallicity interpolation coefficients of the spectral synthesis, with linear interpolation in the first age cell. Bins are then merged at age boundaries of 1 and 5 Gyr, metallicity boundaries of 0.008 and 0.02, and velocity boundaries of $-200, -100, 0, 100, 200$ km s^{-1}. The outer velocity bins include the distribution tails. Particle velocities are unchanged; exact Gaussian integrals are used for the model. The coarser-grid test retains the age boundary at 5 Gyr and the velocity boundaries at ± 100 km s^{-1}. Optical-luminosity, r-band-luminosity and BC03-current-mass weights are considered separately; TNG particle masses provide a separate physical reference. The SSP weights describe the intrinsic population before the common continuum polynomial is applied.

To test composition, we use either the four spectra of entire families or up to 48 spectra of their parts. Each family is divided at original particle ages of 5 Gyr, metallicity 0.02 and velocities of ± 100 km s^{-1}. The sum of the parts reproduces the original family spectrum. For the spectrum S_c of part c, an admissible mixture satisfies

$$\left| \sum_c \alpha_{kc} S_c(\lambda) - C_k(\lambda) \right| \leq \delta s(\lambda), \qquad \alpha_{kc} \geq 0, \qquad \sum_k \alpha_{kc} = 1. \tag{6}$$

All components are constrained simultaneously. With $F_c = \int S_c \, d\lambda$, the retrograde flux fraction in a component is

$$f_{\mathrm{CR},k} = \frac{\sum_{c \in \mathrm{CR}} \alpha_{kc} F_c}{\sum_c \alpha_{kc} F_c}. \tag{7}$$

The minimum and maximum of this fraction are found by linear-fractional optimization with a variable denominator. If the admissible component normalization

can vanish, the fraction is undefined. We also find the smallest admissible $\delta_{\min}$. The total-spectrum residual provides a lower bound:

$$\delta_{\min} \geq \frac{1}{K} \max_{\lambda} \frac{|\sum_k C_k(\lambda) - \sum_c S_c(\lambda)|}{s(\lambda)}. \tag{8}$$

Refining the set of parts and increasing the tolerance cannot narrow the admissible range. These conditions are checked in the calculation.

A.6 Mass-error decomposition

For the energy-integrated component flux F in the stated window,

$$\log_{10} \frac{M_{\rm fit}}{M_{\rm CR,TNG}} = \log_{10} \frac{F_{\rm fit}}{F_{\rm CR}} + \log_{10} \frac{M_{\rm fit}/F_{\rm fit}}{M_{\rm CR,BC03}/F_{\rm CR}} + \log_{10} \frac{M_{\rm CR,BC03}}{M_{\rm CR,TNG}}. \tag{9}$$

The identity directly compares recovered and true quantities. Its terms can cancel and are not independent causes of error. Isolated-family spectra provide a further reference under the same observing conditions.

A.7 Observable diagnostics

The local sign test requires two opposite-sign profiles in each aperture, separated by at least 25 km s^{-1}, each carrying at least 0.01 of the energy-integrated flux. It does not track one population between apertures.

For the mass-consistency check, two distinct 3G profiles are matched to the two 2G profiles by minimum total Hellinger distance, using fitted profiles alone. Ambiguous assignments, nonpositive masses or amplitudes, and numerical failures prevent comparison. The warning is $|\log_{10}(M_{2G}/M_{3G})| > 0.3$ dex. Its evaluation uses the physically matched 2G component and asks whether the warning accompanies $|\log_{10}(M_{2G}/M_{\rm CR,TNG})| > 0.3$ dex.

B Sensitivity of the physical-recovery comparison

Table 5 shows how many apertures allow the matched component's properties to be evaluated, and how errors change on common apertures of the six disc systems. Each variant is compared with the regular model of the same component count, except for the explicit 2G–3G row. All comparisons use $i = 60°$, 4×1800 s and spectra without added noise. Error changes are computed only for apertures with estimates in both models. There are no such apertures in the E-MILES 3G row: the alternative model's two estimates concern apertures where no component can be selected in the baseline.

B.1 Sensitivity of the numerical solution

For the two exposures without added noise, the input spectra are bitwise identical and the assigned uncertainties differ by exactly a factor of two. In the most sensitive common eligible case, the first aperture of 671904 at 80° with 3G, age changes by

Table 5 Sensitivity relative to the baseline. N counts estimates from the alternative model included in the comparison with the retrograde family; B, L and G count apertures with estimates in both models, only the baseline, and only the alternative. n_g counts galaxies with estimates in both models. ΔA and ΔM are equally weighted means of within-galaxy medians of the change in absolute error, in Gyr and dex. Negative values indicate smaller errors. The LSF 6.0 case changes both input and model; 3.78 and 4.62 change only the fitted LSF. PSF is in arcsec, LSF in Å, and the dispersion bound in km s^{-1}.

Variant	Model	N	B	L	G	n_g	ΔA	ΔM
2G → 3G	3G	8/12	6	4	2	3	-0.379	-0.018
PSF 1.5	2G	8/12	8	2	0	4	+0.027	+0.000
LSF 6.0	2G	8/12	8	2	0	4	+0.080	-0.007
PSF 1.5	3G	8/12	8	0	0	4	+0.025	-0.004
LSF 6.0	3G	8/12	8	0	0	4	+0.227	+0.003
E-MILES	2G	4/12	4	6	0	2	-0.288	+0.095
E-MILES	3G	2/12	0	8	2	0	–	–
LSF 3.78	2G	10/12	10	0	0	5	+0.071	+0.000
LSF 3.78	3G	8/12	8	0	0	4	+1.646	+0.096
LSF 4.62	2G	8/12	8	2	0	4	-0.086	+0.019
LSF 4.62	3G	6/12	4	4	2	2	+0.328	+0.119
$\sigma_3 \geq 80$	3G	8/12	4	4	4	2	+0.075	-0.004

Table 6 Baseline recovery in the six disc systems. N_0 and N_n count estimates included in the comparison with the original retrograde family, without added noise and with three noise realizations, respectively. G_n counts the galaxies represented among noisy estimates. For A_n and M_n, median absolute age and mass errors are first computed within each galaxy and then averaged with equal galaxy weights. Because the galaxy and aperture sets differ, differences between these means do not measure error changes on a common set. Exposure e is in units of 1800 s.

i	e	Model	N_0	N_n	$G_n/6$	A_n (Gyr)	M_n (dex)
60	4	2G	10/12	14/36	3/6	0.291	0.155
60	4	3G	8/12	12/36	3/6	0.626	0.217
60	16	2G	10/12	16/36	4/6	0.972	0.151
60	16	3G	8/12	8/36	3/6	1.543	0.193
80	4	2G	10/12	18/36	4/6	1.356	0.168
80	4	3G	10/12	16/36	4/6	1.522	0.213
80	16	2G	10/12	24/36	4/6	1.667	0.155
80	16	3G	10/12	12/36	3/6	1.059	0.102

0.435 Gyr and mass by 0.048 dex. After rescaling to the same uncertainties, the full χ^2 is 0.003255 and 0.002545 for the shorter and longer exposures, respectively. The search therefore yields different numerical solutions. With an objective-function tolerance of 10^{-9}, this search terminated at the parameter-change tolerance of 10^{-4}.

Population sensitivity is also present among saved solutions from different initial guesses. In the first aperture of 184947 at 60° and 4×1800 s without added noise, two 3G solutions with similar selected profile velocities (87.76 and 87.54 km s^{-1}) differ by 0.480 Gyr in age and 0.068 dex in mass for a difference of $\chi^2 = 1.27 \times 10^{-6}$. The profiles are matched between solutions by their kinematics; physical matching was not checked again for the alternative solution. This is an example of search sensitivity in the joint spectral model, not an isolated uncertainty estimate for the SSP weights. The finite set of initial guesses does not define confidence intervals or establish that the selected minimum is global.

In the six disc systems at 60° and 4×1800 s, increasing the matching tolerance from 10^{-6} to 10^{-2} leaves the accepted estimates unchanged, both with and without noise. Among accepted noisy 3G pairs, the smallest advantage of the joint choice is 0.027; a tolerance of 0.05 retains four of the six pairs. Checking fixed solutions does not establish identification robustness under new noise.

References

Bacon R, Copin Y, Monnet G, et al (2001) The SAURON project – I. the panoramic integral-field spectrograph. Monthly Notices of the Royal Astronomical Society 326(1):23–35. https://doi.org/10.1046/j.1365-8711.2001.04612.x

Bottrell C, Hani MH (2022) Realistic synthetic integral field spectroscopy with RealSim-IFS. Monthly Notices of the Royal Astronomical Society 514:2821–2838. https://doi.org/10.1093/mnras/stac1532

Bruzual G, Charlot S (2003) Stellar population synthesis at the resolution of 2003. Monthly Notices of the Royal Astronomical Society 344:1000–1028. https://doi.org/10.1046/j.1365-8711.2003.06897.x

Bugueño MC, Gómez FA, Dolfi A, et al (2026) Origins of coplanar counterrotating stellar disk components in late-type galaxies. I. identification, characterization, and formation mechanisms of coplanar counterrotating stellar disk components. Astronomy and Astrophysics 707:A51. https://doi.org/10.1051/0004-6361/202557544

Cappellari M (2017) Improving the full spectrum fitting method: accurate convolution with Gauss–Hermite functions. Monthly Notices of the Royal Astronomical Society 466:798–811. https://doi.org/10.1093/mnras/stw3020

Cappellari M (2023) Full spectrum fitting with photometry in PPXF: stellar population versus dynamical masses, non-parametric star formation history and metallicity for 3200 LEGA-C galaxies at redshift $z \approx 0.8$. Monthly Notices of the Royal Astronomical Society 526:3273–3300. https://doi.org/10.1093/mnras/stad2597

Coccato L, Morelli L, Corsini EM, et al (2011) Dating the formation of the counter-rotating stellar disc in the spiral galaxy NGC 5719 by disentangling its stellar populations. Monthly Notices of the Royal Astronomical Society 412:L113–L117. https://doi.org/10.1111/j.1745-3933.2011.01016.x

Coccato L, Morelli L, Pizzella A, et al (2013) Spectroscopic evidence of distinct stellar populations in the counter-rotating stellar disks of NGC 3593 and NGC 4550. Astronomy and Astrophysics 549:A3. https://doi.org/10.1051/0004-6361/201220460

Coccato L, Fabricius M, Morelli L, et al (2015) Properties and formation mechanism of the stellar counter-rotating components in NGC 4191. Astronomy and Astrophysics 581:A65. https://doi.org/10.1051/0004-6361/201526560

Emsellem E, Cappellari M, Peletier RF, et al (2004) The SAURON project – III. integral-field absorption-line kinematics of 48 elliptical and lenticular galaxies. Monthly Notices of the Royal Astronomical Society 352(3):721–743. https://doi.org/10.1111/j.1365-2966.2004.07948.x

Genel S, Fall SM, Hernquist L, et al (2015) Galactic angular momentum in the Illustris simulation: Feedback and the Hubble sequence. The Astrophysical Journal Letters 804:L40. https://doi.org/10.1088/2041-8205/804/2/L40

Harborne KE, Serene A, Davies EJA, et al (2023) SimSpin v2.6.0—constructing synthetic spectral IFU cubes for comparison with observational surveys. Publications of the Astronomical Society of Australia 40:e048. https://doi.org/10.1017/pasa.2023.47

Ikhsanova A, Costantin L, Pizzella A, et al (2025) From simulations to observations: Methodology and data release of mock TNG50 galaxies at $0.3 < z < 0.7$ for WEAVE-StePS. Astronomy and Astrophysics 703:A37. https://doi.org/10.1051/0004-6361/202555132

Johnston EJ, Merrifield MR, Aragón-Salamanca A, et al (2013) Disentangling the stellar populations in the counter-rotating disc galaxy NGC 4550. Monthly Notices of the Royal Astronomical Society 428:1296–1302. https://doi.org/10.1093/mnras/sts121

Nanni L, Thomas D, Trayford J, et al (2022) iMaNGA: mock MaNGA galaxies based on IllustrisTNG and MaStar SSPs – I. construction and analysis of the mock data cubes. Monthly Notices of the Royal Astronomical Society 515:320–338. https://doi.org/10.1093/mnras/stac1531

Nanni L, Thomas D, Trayford J, et al (2023) iMaNGA: mock MaNGA galaxies based on IllustrisTNG and MaStar SSPs – II. the catalogue. Monthly Notices of the Royal Astronomical Society 522:5479–5499. https://doi.org/10.1093/mnras/stad1337

Nelson D, Pillepich A, Springel V, et al (2019a) First results from the TNG50 simulation: galactic outflows driven by supernovae and black hole feedback. Monthly Notices of the Royal Astronomical Society 490:3234–3261. https://doi.org/10.1093/mnras/stz2306

Nelson D, Springel V, Pillepich A, et al (2019b) The IllustrisTNG simulations: public data release. Computational Astrophysics and Cosmology 6:2. https://doi.org/10.1186/s40668-019-0028-x

Pillepich A, Nelson D, Springel V, et al (2019) First results from the TNG50 simulation: the evolution of stellar and gaseous discs across cosmic time. Monthly Notices of the Royal Astronomical Society 490:3196–3233. https://doi.org/10.1093/mnras/stz2338

Rubino M, Pizzella A, Morelli L, et al (2021) Detectability of large-scale counter-rotating stellar disks in galaxies with integral-field spectroscopy. Astronomy and Astrophysics 654:A30. https://doi.org/10.1051/0004-6361/202140702

Sánchez SF, García-Benito R, Zibetti S, et al (2016) CALIFA, the Calar Alto Legacy Integral Field Area survey. IV. third public data release. Astronomy and Astrophysics 594:A36. https://doi.org/10.1051/0004-6361/201628661

Tabor M, Merrifield M, Aragón-Salamanca A, et al (2019) SDSS-IV MaNGA: full spectroscopic bulge-disc decomposition of MaNGA early-type galaxies. Monthly Notices of the Royal Astronomical Society 485(2):1546–1558. https://doi.org/10.1093/mnras/stz431

Vazdekis A, Koleva M, Ricciardelli E, et al (2016) UV-extended E-MILES stellar population models: young components in massive early-type galaxies. Monthly Notices of the Royal Astronomical Society 463:3409–3436. https://doi.org/10.1093/mnras/stw2231

Zhu L, van de Ven G, Leaman R, et al (2020) Disentangling the formation history of galaxies via population-orbit superposition: method validation. Monthly Notices of the Royal Astronomical Society 496:1579–1597. https://doi.org/10.1093/mnras/staa1584

Statements and Declarations

Funding. This research was carried out within the framework of the state assignment of M. V. Lomonosov Moscow State University.

Competing interests. The authors declare no competing interests.

Data availability. The TNG50-1 simulation data and supplementary catalogues used in this study are publicly available through the IllustrisTNG data portal (https://www.tng-project.org/data/; Nelson et al. 2019b). Access requires registration. The synthetic observations, spectral-fit results and derived tables produced in this study are available from the corresponding author on request.

Code availability. The analysis and figure-generation code is available from the corresponding author on request.

Author contributions. All authors contributed to the scientific design, interpretation of the results, and preparation of the manuscript.